HHS Public Access

Author manuscript

IEEE Trans Biomed Circuits Syst. Author manuscript; available in PMC 2019 October 01.

Published in final edited form as:

IEEE Trans Biomed Circuits Syst. 2018 October ; 12(5): 1100–1111. doi:10.1109/TBCAS.2018.2871470.

End-to-End Design of Efficient Ultrasonic Power Links for Scaling towards Sub-Millimeter Implantable Receivers

Ting Chia Chang [Student Member, IEEE], **Marcus J. Weber [Student Member, IEEE]**, **Jayant Charthad [Student Member, IEEE]**, **Spyridon Baltsavias [Student Member, IEEE]**, and **Amin Arbabian [Senior Member, IEEE]**

Electrical Engineering Department, Stanford University, Stanford, CA 94305 USA

Abstract

We present an analytical framework for optimizing the efficiency of ultrasonic wireless power links for implantable devices scaled down to sub-mm dimensions. Key design insights and tradeoffs are considered for various parameters including the operating frequency, the transmission depth, the size of the transmitter, the impedance and the aperture efficiency of the miniaturized receiver, and the interface between the receiver and the power recovery chain on the implant. The performance of spherically focused transducers as ultrasonic transmitters is analyzed to study the limits and the tradeoffs. Two optimization methods are presented: “Focal Peak” sets the focus of transducers at target depths, and “Global Maximum” maximizes the efficiency globally with off-focus operation. The results are also compared to phased array implementations. To investigate the efficiency of implants, miniaturized receivers made from single crystalline piezoelectric material, PMN-PT, are used as they have resonances in the derived optimal carrier frequency range (~ l-2 MHz). A methodology to achieve an efficient interface to the power electronics is then provided using an optogenetic stimulator as an example platform. The analytical results are verified through both simulations and measurements. Finally, an example ultrasonic link using a spherical transmitter with a radius of 2 cm is demonstrated; link efficiencies of 1.93–0.23% are obtained at 6–10 cm depths with sub-mm receivers for the optogenetic application.

Index Terms:

implantable devices; ultrasonic power transfer; wireless power transfer; link efficiency; miniaturized receivers; spherically focused transducer; phased array; single crystalline piezoelectric materials; optogenetic stimulators

I. Introduction

Miniaturization of implantable devices can allow for less invasive surgical procedures, reduce damage to the surrounding tissue, and potentially open up new medical applications [1]–[4], To achieve this goal, wireless powering of implants to eliminate batteries has been of significant interest over the past decade [5]–[8], There have been many research efforts on inductive and capacitive coupling [8]–[10], RF-based radiative power transfer [6], [11], and optical techniques [12], Alternatively, power delivery using ultrasound (US) has recently been shown as a promising approach [7], [13]–[18]. US has several advantages including superior transduction efficiency and energy focusing as a result of mm wavelength [7], [19],

low tissue attenuation (0.5–1.0 $dB \cdot cm^{-1} \cdot MHz^{-1}$) [20], and high safety limit (7.2 mW/mm^2) [21], With these advantages, mm-sized US-powered implants through deep tissue have been demonstrated in [7], [22]–[27] for different applications.

A conceptual diagram of an implant system with an US power link is shown in Fig. 1. A US transmitter (TX), which can be implemented using a single element transducer or an array, is placed on or under the skin. Acoustic power is transmitted wirelessly from the TX and harvested by the US receiver (RX) on the implant embedded in tissue. Depending on the applications, implants may require power levels ranging from several μWs (sensing or monitoring) to several mWs (stimulation). Analysis of various aspects of US links and its transfer efficiency have been previously addressed in the literature [13]-[17], [28], Many of these works rely on the transmission line based one-dimensional (ID) models [13], [28]; however, these models do not take into account the effects of focusing or diffraction of US waves as well as scaling of the RX. In [14], analysis is presented to study the performance of the RX, but it does not include the discussion of the TX. In [15], [16], designs of US links are demonstrated using specific examples, and both have large RXs (> 50 mm^2); thus, design insights for miniaturized implants are lacking. Further, in [17], optimization of the US link is shown using simulations, it lacks an analytical study for design intuition; the discussion in [17] is also limited toflat, single-element transducers without considerations of focused transducers or arrays on the TX side.

In this paper, we present an analytical framework to compute and optimize the efficiency of US links when the implant is aggressively scaled down to mm or sub-mm dimensions. The framework provides key design insights for both US TX and RX with considerations of various design parameters. We will discuss two optimization procedures; the optimal operating frequency and the associated efficiency will be shown for given transmission distances and TX/RX sizes for both methods. We also include, and further expand on, the work in [18] to show the end-to-end link efficiency of an example optogenetic application. This framework can be extended to other US power applications with different constraints and specifications.

In section II, we introduce the expression of the overall US link efficiency and explain the individual components involved in the link. A spherically focused transducer, acting as an ideal TX, is analyzed and compared with the simulations for two methods in section III. Tradeoffs between TX aperture size, operating frequency, and power transfer depth are discussed. In section IV, we show the design methodology of scaled RXs with piezoelectric materials in the context of the entire US link such that they fall in the optimal frequency range and have favorable impedances. In addition, the harvesting capability of scaled RXs and the efficiency of the complete power recovery chain of an implantable optogenetic stimulator are investigated. Finally, we combine the analysis of TX and RX in section V and present the end-to-end efficiency of an example US link.

II. US Link Efficiency

For power transfer to miniaturized implants, a RX is typically placed near or beyond the focus of a TX, and the wireless link operates in the radiative near-field or far-field. Since the

US TX and RX have significant size difference, the direct coupling, as is common with power transfer using large inductive coils, is minimal [8], [29], [30], Therefore, the overall US link efficiency, η_{US}, can be generalized as the product of two independent terms,

$$\eta_{US} = \eta_{focus,TX} \cdot \eta_{implant} = \frac{P_{acou,RX}}{P_{acou,TX}} \cdot \frac{P_L}{P_{acou,RX}}, \quad (1)$$

where $\eta_{focus,TX}$ is the focusing efficiency of the TX, which can be expressed as the total acoustic power incident on the RX, $P_{acou,RX}$, divided by the total acoustic power emitted from the TX, $P_{acou,TX}$; $\eta_{implant}$ is the efficiency of the implant to convert $P_{acou,RX}$ to the electrical power delivered to the medical payload, P_L. Both efficiency terms are illustrated in Fig. 1. $\eta_{focus,TX}$ is determined mainly by twofactors, the ability of the TX tofocus the beam and the propagation losses in the medium. The first is related to the geometry, the aperture, the phases of the array elements, and the operating frequency. The latter is associated with the tissue type as well as the operating frequency and the transmission distance; the attenuation in a typical medium is about 0.5–1.0 $dB \cdot cm^{-1} \cdot MHz^{-1}$ forplane wave propagation [20], $\eta_{implant}$ is a function of the characteristics of the RX, impedance matching between the RX and the electronics, and the efficiency of AC to DC conversion circuits which further depends on the electrical load [7], Note that (1) does not include the electrical-acoustic conversion efficiency of the TX as it depends on the materials, the resonance, and the acoustic design of transducers; transducers with electrical-acoustic conversion efficiency as high as 85% have been reported [31], [32], Furthermore, overhead power from control circuits and power amplifiers driving the TX are also excluded in (1) since they are dependent on the specific circuit implementations which have been discussed in the literature [16], [33], [34].

III. Focusing Efficiency of a US Transmitter

In order to optimize $\eta_{focus,TX}$, a US TX should have a large focusing gain or a more confined beam. This can be achieved by using higher operating frequencies or larger apertures for a given transmission depth [35], [36], However, the attenuation in the medium becomes more severe at higher frequencies, and the utilization of large transducers may present practical challenges. There is also a tradeoff between efficiency and alignment; when the beam emitted from a TX is more focused, the link becomes more sensitive to the alignment. To study the limits and the tradeoffs, we analyze a spherically focused transducer with analytical calculations and simulations using Field II [37], [38], This gives an upper bound on the link performance. We then consider a more practical scenario when the TX is a two-dimensional (2D) transmitter array, which is capable of adjusting the US beam electrically to different locations, similar to arrays used for medical imaging [33], [39].

A. Analysis of Spherically Focused Transducers

Fig. 2 (a) illustrates a spherically focused transducer used as aUS TX. The transducer has a circular aperture with a radius a and is assumed to have a uniform normal displacement velocity, μ_0, on the surface. The radius of curvature or the geometrical focus of a transducer,

R_a, determines the location of the focus. h is the distance between the center of the transducer surface and the center of its circular aperture plane (point c_a in Fig. 2 (a)). The focusing strength of a transducer is characterized by $a^2/\lambda R_a$, where λ is the wavelength [35], [40]. We define the transmission depth through tissue, d, from the circular aperture plane to the location of the implant as seen in Fig. 2 (a). $P_{acou,TX}$ for a transducer with μ_0 on the surface can be calculated by,

$$P_{acou,TX} = \mu_0^2 Z_0 \pi\left(a^2 + h^2\right), \quad (2)$$

where Z_0 is the acoustic impedance of the medium and $\pi(a^2+h^2)$ is the total surface area of the transducer. Fig. 2 (b) shows an example of simulated normalized acoustic intensity at 1.0 MHz in the xz-plane using parameters of a = 2 cm, R_a = 5 cm, and μ_0 = 5 mm/s in homogeneous tissue with 0.8 dB/cm attenuation. The US beam is focused at 4.75 cm away from the surface of the TX, slightly smaller than the geometrical focus of 5 cm due to diffraction and attenuation [35], [40], [41]; thus, R_a should be tuned accordingly if one wants to place the actual focus at the desired location.

To calculate $P_{acou,RX}$, it is necessary to know the acoustic intensity, I_{acou}, in terms of power per unit area, incident on the RX as well as the relationship between the associated beam size and the area of the RX, A_{RX}. I_{acou} along the z axis of a spherically focused transducer in an attenuating medium is analytically derived in [42],

$$I_{acou}(z) = \frac{p(z)^2}{\rho_0 c_0} = \frac{p(z)^2}{Z_0}\left|\frac{\rho_0 \omega \mu_0}{k_c}\frac{R_a}{R_a - z}e^{-ik_c z}\left(1 - e^{-ik_c \beta(z)}\right)\right|^2 / Z_0, \quad (3)$$

$$\beta(z) = \sqrt{z^2 + 2h\left(R_a - z\right)} - z, \quad (4)$$

$$h = R_a - \sqrt{R_a^2 - a^2}, \quad (5)$$

$$k_c = k - i\alpha, \quad (6)$$

where p is the pressure along the z axis, ρ_0 and c_0 are the density and the sound velocity of the medium, ω is the frequency, and k_c is the complex wavenumber containing the attenuation coefficient of the medium, α. Equation (3) is more accurate around and beyond the focus. Note that wave propagation in tissue is typically considered as linear for pressure amplitudes used in US wireless power transfer and in this work [36]. The shape of the main

beam at and beyond the focal plane can be approximated by the square of a Jinc function [35], [42],

$$\mathrm{Jinc}^2\left(2\pi\frac{ar}{\lambda d}\right)=\left(2J_1\left(2\pi\frac{ar}{\lambda d}\right)/\left(2\pi\frac{ar}{\lambda d}\right)\right)^2 \quad (7)$$

where r is the distance from the center of the plane of interest and J_1 is the order-one Bessel function of the first kind. With the knowledge of I_{acou} and the shape of the beam in the plane, $P_{acou,RX}$ can be approximated based on the 'cone' model shown in Fig. 3. The bottom of the cone is the plane of interest and the tip of the cone represents the maximum I_{acou} in the plane; as a result, the volume of the cone is equal to the total acoustic power within the main beam. If Arx is smaller than the beam, $P_{acou,RX}$ is computed by integrating I_{acou} incident only on the RX (partial volume of the cone); otherwise, $P_{acou,RX}$ is the total acoustic power contained in the beam (total volume of the cone). Because of this approximation, the error in $P_{acou,RX}$ increases when the beam is comparable to or smaller than A_{RX}.

To investigate how the choice of Ra impacts the link efficiency, we look at an example scenario where the target transmission depth is 8 cm. Using the same parameters in Fig. 2 (b), R_a is adjusted to 10.2 cm to set the actual focus to 8 cm; the normalized I_{acou} along the z axis is shown as the blue curve in Fig. 4 (a). But if operating off the focal point and having spots with intensities larger than the location of the RX in the field is acceptable for the intended applications, a different R_a should be chosen in order to maximize the efficiency globally. As seen in Fig. 4 (a), with the same $P_{acou,TX}$, the TX with an R_a of 8.3 cm has an I_{acou} 1.39× higher than the one with an R_a of 10.2 cm at the same depth of 8 cm. This is because the TX with smaller R_a has larger focusing strength at the same operating frequency. Since the simulated lateral beam profiles at the 8 cm plane are similar for both cases, as plotted in Fig. 4 (b), it is preferable to utilize a TX with an R_a of 8.3 cm in this example to maximize $\eta_{focus,TX}$ for mm-sized RXs. A downside of going for the smaller R_a is that the link becomes slightly more sensitive in the z direction as the gradient of the intensity curve is not 0; nevertheless, even with small perturbations in z, higher efficiency can still be achieved by operating off the focus. Fig. 4 (c) shows the comparison between the calculated R_a versus depths for setting the focus at the target depths, "Focal Peak (FP)," and for maximizing efficiency globally, "Global Maximum (GM)". For shallow depths, R_a are close for both cases; but they start deviating for larger depths and the ratio of intensity between the two increases as shown in Fig. 4 (d).

We are now ready to optimize $\eta_{focus,TX}$ across frequencies using both the FP and GM methods. The procedure for FP is as follows: for a given target transmission depth and a TX size, the location of the actual focus that is equal to the depth is first found by sweeping R_a; then $P_{acou,RX}$ is calculated based on the corresponding I_{acou} and the beam profile with the given A_{RX}; finally, $\eta_{focus,TX}$ is computed by dividing the calculated $P_{acou,RX}$ by the associated $P_{acou,TX}$·For GM, $P_{acou,RX}$ for different R_a is computed based on I_{acou}, the given A_{RX}, and the beam profile; then maximum $\eta_{focus,TX}$ at each frequency is selected. Here, we consider a from 1 to 3 cm since it is a reasonable range for a wearable TX or a TX implanted

under the skin. Castor oil, which has similar acoustic properties to tissue (ρ_0= 0.93 g/cm^3, Z_0 = 1.40 MRayls, and an approximated α = 0.8 dB·cm^{-1}·MHz^{-1}) is used as the medium to be consistent with the measurement environment. A_{RX} is assumed to be a 1.0 mm^2 disk as an example miniaturized RX on in this section ($\eta_{focus,TX}$ for different A_{RX} will be discussed in section V).

Fig. 5 plots the calculated $\eta_{focus,TX}$ across frequencies of two optimizations for three different values of a and for two example depths of 6 and 10 cm. The simulated $\eta_{focus,TX}$ are also shown for a TX with an a of 2.0 cm in the figure. $P_{acou,RX}$ in the simulation is computed by integrating I_{acou} numerically over the entire A_{RX} instead of using the cone model. The simulations agree well with the analytical calculations; small deviations are seen at high frequencies since the beamwidth is close to size of the RX. Several observations can be made from Fig. 5 for both the FP and GM methods. First, there is a fundamental tradeoff between focusing gain and propagation loss for a given aperture size; for lower frequencies, $\eta_{focus,TX}$ drops due to smaller focusing strength even though the attenuation is lower; for higher frequencies, $\eta_{focus,TX}$ decreases because the attenuation increases. Second, the optimal frequency, f_{opt}, lies around 1 to 2 MHz for maximum $\eta_{focus,TX}$, and it decreases for larger transmission depth due to the increasing losses. Third, a TX with a larger aperture gives higher $\eta_{focus,TX}$ and has lower f_{opt} because its focusing strength is stronger at lower frequencies. Based on the discussion above, one can expect that a medium with a larger attenuation coefficient will decrease $\eta_{focus,TX}$ and f_{opt}. In addition, when A_{RX} is scaled down, $\eta_{focus,TX}$ will drop due to a smaller power receiving area.

Fig. 5 also shows the comparison between the results of the FP and GM optimizations. $\eta_{focus,TX}$ obtained by GM is higher than $\eta_{focus,TX}$ from FP across all frequencies though the difference becomes negligible with large TXs and small transmission depths. As mentioned previously, one should consider intensities at other locations for GM due to off-focus operation. Large differences in $\eta_{focus,TX}$ are observed between the two methods for small a since placing the actual focus at the desired depth requires large R_a for a given frequency which results in weaker focusing. As seen in Fig. 5 (b), the FP algorithm is not able to focus to 10 cm depth at low frequencies for an a of 1 cm. In order to make comparison to GM, we also plot $\eta_{focus,TX}$ of an unfocused TX (i.e. R_a is infinite). In this case, the RX is also operated off the peak intensity point. The optimal $\eta_{focus,TX}$ for this TX is 0.16% achieved at 0.82 MHz, which is still lower than 0.22% obtained from GM.

Table I summarizes the details at the optimal points for both depths. For an a of 3.0 cm, $\eta_{focus,TX}$ with the GM method can reach 7.51% for a depth of 6 cm and 1.62% for a depth of 10 cm with an A_{RX} of 1 mm^2, indicating that the US TX can efficiently transfer power through large depths of tissue to power up mm-sized implants. The calculated and simulated half-power beam widths at the operating point, $w3dB$, are also shown in Table I. For the calculation, w_{3dB} is approximated with $0.51\lambda d/a$ by setting (7) to 0.5; compared to the simulated values, calculated w_{3dB} is slightly underestimated. For the examples in Table I, w_{3dB} are larger than RX sizes of interest, particularly for 10 cm depth; thus, the link is not extremely sensitive to the lateral alignment between the TX and the RX. Tofurther mitigate the sensitivity to the alignment, one can choose to use a TX with a smaller aperture or shift to a lower operating frequency (w_{3dB} is inversely proportional to frequency), directly trading

off with efficiency; closed-loop controls can also be implemented to ensure the alignment [43].

Using the optimization algorithms for the FP and GM methods, optimal $\eta_{\text{focus,TX}}$ across transmission depths for three apertures with an A_{RX} of 1 mm^2 can be found (Fig. 6). As expected, shallow depths and larger apertures achieve higher $\eta_{\text{focus,TX}}$ with the tradeoff of smaller beamwidth; $\eta_{\text{focus,TX}}$ of 20% is obtained for an a of 3.0 cm at a depth of 3 cm. Comparing FP and GM for a given TX size, $\eta_{\text{focus,TX}}$ deviates more for larger depths. Particularly, for an a of 1.0 cm, $\eta_{\text{focus,TX}}$ from FP drops at a steeper rate because higher operating frequency is required to set the focus, resulting in larger attenuation; as a consequence, focal points of the TX with an a of 1.0 cm beyond 6 cm transmission depths do not necessarily have the highest intensity in the field.

B. Measurement of Spherically Focused Transducers

To confirm the analysis, we measure the intensity profiles of two focused transducers with an a of 2.0 cm but different focusing depths (Olympus 392). These transducers achieve focusing through the use of acoustic lenses. Although they are not constructed with spherically curved crystals as depicted in Fig. 2 (a), [44] shows that the analytical model can still be applied by correcting the radius of curvature of the transducers. Therefore, we first conduct measurements in water (medium with negligible attenuation) to estimate R_{a} and find the electrical-to-acoustic conversion efficiency which includes the effects of imperfect geometry and non-uniform displacement on the surface as well as losses through the backing, the matching layers, the acoustics lens, and the material. I_{acou} of both transducers are mapped using the hydrophone (Onda HNC-1500) controlled by linear stages in a tank. Two transducers are estimated to have R_{a} of 6.8 and 12.5 cm respectively, and the electrical-to-acoustic conversion efficiencies are about 10%. The conversion efficiency is low for these transducers because they are built for imaging applications rather than power transfer, trading off efficiency for wider bandwidth. As the optimized $\eta_{\text{focus,TX}}$ for the FP and GM methods in Fig. 5 has an associated R_a at different frequencies, for 6 cm depth, we can verify $\eta_{\text{focus,TX}}$ for FP at the operating frequency of 1.20 MHz for the TX with an R_{a} of 6.8 cm. For depth of 10 cm, 1.40 MHz is chosen for the TX with an R_{a} of 12.5 cm to compare to $\eta_{\text{focus,TX}}$ obtained from the FP optimization. Fig. 7 shows the measured normalized I_{acou} along the z axis in castor oil for both TX at 1.20 MHz and 1.40 MHz, respectively. The measurements match well with the analytical solutions near the focusing region, though small deviations are observed in the near field due to the difference in geometry. Fig. 7 also shows that the 3-dB depth of field (DOF) is more than 2 cm, indicating small misalignments in z will not result in large degradation in $\eta_{\text{focus,TX}}$. The measured $\eta_{\text{focus,TX}}$ is 3.5% for the transducer with an R_{a} of 6.8 cm at a depth of 6 cm compared to 4.0% from the analytical solution. For the other transducer, 0.32% is measured at a depth of 10 cm while the calculation from FP gives 0.48%. The measured $\eta_{\text{focus,TX}}$are close to the predicted values but slightly lower because the attenuation in castor oil may be higher than estimated and the pressure sensitivity of the hydrophone, which is reported in water, may change slightly when the hydrophone is used in castor oil. Additionally, we measure w_{3dB} for both transducers, the first transducer has a w_{3dB} of 2.10 mm and the other one has a w_{3dB} of 3.20 mm; they are comparable to 2.06 mm and 2.90 mm from the Field II simulation.

C. Comparison to Two-Dimensional Arrays

Although spherically focused transducers can be used for power transfer, the lack of flexibility to adjust the focal point in real time can be detrimental when the channel changes, for example, due to implant movements. A ID or 2D phased array, on the other hand, is preferred in practice as it can mitigate this issue by electronically beamforming to different locations to maintain high power transfer efficiency. The beamwidth can also be adjusted to alleviate alignment sensitivity by tuning the phase of each element intelligently [39]. Furthermore, if multiple implants are deployed in the body, a TX array can address and network them simultaneously or by using time division multiplexing [43]. Nonetheless, there are drawbacks when using a TX array. One important example is that the focusing gain of an array is degraded compared to a spherically focused transducer with similar dimensions. This is due to the finite dimension of the array elements, limiting the accuracy of the resulting curvature.

To illustrate, we compare a spherically focused TX with the same parameters used in Fig. 2 (b) to two rectangular 2D arrays without an acoustic lens that have similar areas (~12.6 cm^2) in the simulation. The first array (Array I) has 46 elements in each row and column with an element width of 0.7 mm and a pitch of 0.77 mm, which is about half of the wavelength at 1.0 MHz for large steering angle capability; the configuration gives a total area about 12.5 cm^2. The second array (Array II) has 23 × 23 elements with an element width of 1.47 mm and a pitch of 1.54 mm. Array II is a more manageable design for fabrication and circuit implementation with the tradeoff of having smaller beamforming angles. Both arrays have their focus set at 4.5 cm so the maximum I_{acou} of each array can be achieved near the actual focus of the spherical TX.

Fig. 8 shows the simulated I_{acou} with the same emitted acoustic power along the z axis for three cases. I_{acou} at the focus for the spherically focused TX is the highest as expected; Array II has slightly lower I_{acou} than Array I since Array II has fewer controllable elements. Maximum I_{acou} for both arrays are about 17% and 27% less than the spherically focused TX respectively. Simulated w_{3dB} are 1.88 mm, 1.83 mm, and 1.88 mm for the three scenarios respectively. Therefore, when an RX is at the focus of a US TX, efficiency of the link will be lower when using a 2D array compared to using a spherically focused TX.

IV. Implant Efficiency with Scaled Receivers

After analyzing the first part of US links, from the external TX focusing down to the RX, we now discuss the efficiency of the implant recovering the incident acoustic power when the RX is scaled down for the purpose of implant miniaturization, $\eta_{implant}$ quantifies the harvesting capability of the US RX and the efficiency of the interface between the RX and the electronics on the implant for a given medical payload. To demonstrate the high power capability of US power delivery, we investigate $\eta_{implant}$ of the implantable optogenetic stimulator described in [24] as an example implant application.

In its simplest form, the power recovery chain of the US-powered optogenetic stimulator includes a US RX made from a piezoelectric material, a full-wave bridge rectifier with Schottky diodes, a capacitor, a current-limiting resistor, and an LED for optical stimulation.

Typically, an LED power of 1 to 6 mW is needed to achieve optical intensities of 1 – 1 5 mW/mm^2 for effective optogenetic stimulation [45]. The circuit schematic is shown in Fig. 9. The Thévenin equivalent model represents an RX operating at its short-circuit resonance frequency, f_{sc} The model consists of an open-circuit peak voltage, V_{oc}, and a short-circuit resistance, R_{sc}. The electrical available power of the RX, $P_{av,elec}$ can be calculated from the received V_{oc} and R_{sc}.

In the steady state, $\eta_{implant}$ is the product of the aperture efficiency of the RX, η_{aper}, the effective impedance matching efficiency between the RX and the rectifier, η_{match}, the efficiency of rectifier, η_{rect}, and the efficiency due to power loss from the current-limiting resistor, η_{res}. Thus, $\eta_{implant}$ can be written as,

$$\eta_{implant} = \frac{P_L}{P_{acou,RX}} = \eta_{aper} \cdot \eta_{match} \cdot \eta_{rect} \cdot \eta_{res}. \quad (8)$$

To analyze and optimize $\eta_{implant}$ while scaling down RXs, we first look at the design of RXs for η_{aper} and the impedance. A ID circuit model is used for first-order analysis and a three-dimensional (3D) finite element method (FEM) is utilized for more accurate modeling. Finally, we provide a system-level analysis, focusing on η_{match}, for the optimization of $\eta_{implant}$.

A. Design and Scaling of Ultrasonic Piezoelectric Receivers

Selections of material and dimensions determine the power harvesting characteristics of the RX made from piezoelectric material. The important metrics for the design are dimensions, resonance frequency, impedance profile, and η_{aper}. We consider the case when the RX is operated at its f_{sc} since no additional electrical matching network is required to efficiently interface with the power recovery circuit, though it is possible to add a simple capacitive matching network at the interface to tune the operating frequency for further optimization as shown in [30].

Based on the results from section III, it is desirable to position f_{sc} of the RX near 1 to 2 MHz for high power transfer efficiency for deep tissue operation. Using the ID model f_{sc} can be approximated by [30], [35],

$$f_{sc} = \left(1 + \frac{8}{\pi^2}\frac{k_{33}^2}{1-k_{33}^2}\right)^{-1/2} \frac{v_p}{2t}, \quad (9)$$

where k_{33} is the electrical-mechanical coupling coefficient, v_p is the sound velocity of the piezoelectric material, and t is the thickness of the material. Equation (9) gives a more accurate result when the RX has cross-sectional dimensions much smaller than its thickness such that mechanical stress from the sides of RX is assumed to be zero (i. e. RX is in the expander bar mode) [35], Materials with lower v_p and larger k_{33} are preferable for miniaturization while maintaining low MHz operation. PZT-based materials have been

adopted for power harvesting applications previously [7], [22]-[26], but they can result in large f_{sc} when the thickness of the RX is scaled down. As an example, we compare single crystal piezoelectric material, PMN-PT [46], along with PZT4 and PZT5H for a thickness of 0.5 mm. From the material properties in Table II and (9), f_{sc} of all three materials can be computed to be 1.57 MHz, 3.07 MHz, and 2.69 MHz respectively. PMN-PT has the lowest f_{sc} as it has larger k_{33} and lower v_p compared to PZT-based materials. Additionally, f_{sc} of the PMN-PT RX falls in the desirable frequency range so it is clearly a more suitable material to use when the dimension is scaled down.

Next, we perform 3D FEM simulation in COMSOL Multiphysics to predict the characteristics of PMN-PT RXs and then verily the results by measurement. In the simulation setup, a block of PMN-PT with thickness of 0.5 mm is instantiated in mineral oil medium using material constants provided by the manufacturer. The width of the block is swept from 0.1 mm to 1.2 mm. An air block is placed underneath the RX to model air backing to increase η_{aper} [47]. The whole structure is enclosed with a perfectly matched layer, and quarter symmetry is utilized to reduce computation time. To verily the simulations, we dice PMN-PT with widths ranging from 0.3 mm to 1.0 mm with 0.1 mm resolution and package them on a flexible printed circuit board as shown in Fig. 10 (a) and (b). Air backing is created by utilizing a stiffener structure. Impedance and power transfer measurements are both done in the custom-designed tank. In order to eliminate the effect of the attenuation and reduce the electrical loading, the tank is filled with mineral oil to characterize the RXs.

The simulated and the measured f_{sc} and R_{sc} of PMN-PT RXs for different widths are plotted in Fig. 11 (a) and (b), respectively. An f_{sc} of 1.54 MHz is obtained for a width of 0.1 mm in simulation, which is close to the value predicted by (9) since the RX with width of 0.1 mm has a rod-like shape. However, (9) does not hold for RXs with larger widths; the down-shift of f_{sc} is observed in simulation and confirmed by measurement. This shift can be explained by the effective reduction of k_{33} and mode coupling [48]. The measured R_{sc} lies in the range of 400 – 5000 Ω and monotonically decreases for increasing widths. The measured R_{sc} closely aligns with the simulated values for widths larger than 0.5 mm, indicating that FEM simulations can be used to design f_{sc} and R_{sc} of RXs with reasonable accuracy. Small deviations between simulation and measurement, particularly for widths of 0.3 mm and 0.4 mm, are likely due to the effects of packaging surrounding the RXs, which are not completely modeled in simulation. The difference is expected to be more significant as the piezo is scaled down to a few 100 μms.

Fig. 11 (c) shows the measured η_{aper} of PMN-PT RXs at their respective f_{sc} as a function of the width. Measurement of η_{aper} captures the effect of the packaging and the interaction of the acoustic field. η_{aper} is defined as,

$$\eta_{aper} = \frac{P_{av,elec}}{P_{acou,RX}} \approx \frac{P_{av,elec}}{I_{acou} A_{RX}}. \quad (10)$$

$P_{acou,RX}$ can be approximated to be the product of the incident I_{acou} and A_{RX} when the incoming wave has w_{3dB} larger than the width of the RXs. Increasing η_{aper} for RX dimensions less than the propagation wavelength, even above 100%, is a well-known phenomenon in antenna and optics theory because RXs can have effective apertures larger than their physical apertures [49], [50]. For devices with widths smaller than 0.5 mm, the measured η_{aper} do not continue to increase because of losses from the packaging and the material itself. We have also plotted $P_{av,elec}$ given an I_{acou} of 1 mW/mm^2 in Fig. 11 (c). $P_{av,elec}$ increases when A_{RX} increases; about 1 mW of $P_{av,elec}$ is achieved for RXs with larger widths. Interestingly, diminishing returns are found in $P_{av,elec}$ for widths larger than 0.6 mm, due to the decreasing η_{aper}.

B. System-Level Analysis of the Optogenetic Stimulator

Besides η_{aper} of scaled PMN-PT RXs, the rest of the efficiency terms in (8) are also required to calculate $\eta_{implant}$ η_{rect} and η_{res} mostly have constant values for the power levels of interest, η_{rect} is measured to be 80% and η_{res} is close to 90% [24]. Nonetheless, η_{match}, defined as,

$$\eta_{match} = \frac{P_{in,elec}}{P_{av,elec}}, \quad (11)$$

where $P_{in,elec}$ is the electrical power flowing into the rectifier, is significantly influenced by the R_{sc} of the RX used; therefore, it requires a careful optimization. Because the rectifier or power harvesting circuit in general is highly non-linear, the effective input impedance, R_{in} (Fig. 9), can vary greatly with power levels. This limits the use of conventional linear circuit power matching theory. As a result, we numerically solve for η_{match} using a time-averaged power calculation, assuming constant diode drops in the rectifier. Optimal R_{sc} for different $P_{av,elec}$ can easily be obtained using this process. Note that the change of f_{sc} from receiver scaling does not impact η_{match} because the effect of input parasitics of the circuit around MHz can be neglected. η_{match} as a function of R_{sc} is shown in Fig. 12 (a) for a few $P_{av,elec}$ values; a maximum η_{match} of 92% can be achieved if the RX has an optimal R_{sc}. η_{match} does not reach 100% due to the non-linear nature of the rectifier. The calculations are verified by SPICE simulations for a $P_{av,elec}$ of 3 mW, which are also plotted in Fig. 12 (a). For a given $P_{av,elec}$, the decrease in η_{match} with large R_{sc} can be attributed to the decrease in the input voltage due to the voltage division across R_{sc} and R_{in}; the rapid drop of η_{match} for smaller R_{sc} is due to the decrease of V_{oc}, which approaches the diode threshold. Fig. 12 (b) shows the calculated optimal R_{sc} as a function of $P_{av,elec}$ from 1 to 10 mW. The shaded region corresponds to the measured R_{sc} range of PMN-PT RXs reported previously. For $P_{av,elec}$ from 2 to 10 mW, an RX can be chosen to achieve optimal η_{match}; for $P_{av,elec}$ less than 2 mW, one can consider using RXs with widths smaller than 0.3 mm, changing thickness of RXs, or operating RXs off resonance with capacitive matching networks as demonstrated in [30].

Using the measured R_{sc} from the results of PMN-PT scaling, the relationship between η_{match} and the width of RXs for three different P_L through LED can be derived. As seen in

Fig. 13 (a), the RXs with larger widths suffer from low η_{match} for P_L lower than 3 mW because their R_{sc} are smaller than the optimal R_{sc}. On the other hand, since the RXs with smaller widths have large R_{sc}, they are not ideal for implants requiring high load powers. Based on the measured R_{sc} and η_{aper} and putting together all the efficiency terms in (8), $\eta_{implant}$ can be computed across widths of RXs. We also perform measurement for a P_L of 6 mW with prototype implants that have the RXs connected to the power recovery chain. Both the calculated and measured results are shown in Fig. 13 (b). $\eta_{implant}$ can be larger than 100% due to high η_{aper} and the trend of $\eta_{implant}$ mainly follows the measured η_{aper} from Fig. 11 (c). Even though the implant is efficient using RXs with width around 0.4 to 0.6 mm, the required I_{acou} to deliver large load power to the LED can increase drastically because small RXs are unable to achieve high $P_{elec,av}$ for a given I_{acou}.·As seen in Fig. 13 (c), for a P_L of 6 mW, the required I_{acou} rises up significantly for RXs with widths smaller than 0.6 mm which may cause heating concerns. For the larger RXs, required I_{acou} stays approximately constant even though $\eta_{implant}$ is lower as higher $P_{elec,av}$ can be obtained due to larger A_{RX}. Taking both $\eta_{implant}$ and the required I_{acou} into account, it is preferable to use the RXs with widths of approximately 0.6 mm or 0.7 mm in this example for the purpose of miniaturization.

V. Discussion

Using the analysis of efficiency for both US TX and US-powered optogenetic stimulators with the scaled RXs, the overall US link efficiency, which is the product of $\eta_{focus,TX}$ and $\eta_{implant}$, can be computed from (1). To find $\eta_{focus,TX}$for different A_{RX}, the FP and GM optimization procedures introduced in section III are used. Fig. 14 shows the calculated $\eta_{focus,TX}$ for the two methods using a spherically focused transducer with an a of 2 cm at 6 cm depth for widths of RXs from 0.4 to 1.0 mm across frequencies. $\eta_{focus,TX}$ for both methods approximately scales with A_{RX}; and f_{opt} is around 1.5 MHz for all widths. This is expected because the beamwidth around f_{opt} is larger than the RX sizes we are considering for miniaturized implants (w_{3dB} ~ 1.6 mm around f_{opt} from Table I). The ratio of $\eta_{focus,TX}$ between GM and FP is 1.09× at 1.5 MHz. Using the corresponding $\eta_{focus,TX}$ for the TX with an a of 2 cm and $\eta_{implant}$ at the respective f_{sc} of RXs from section IV, the end-to-end link efficiency, η_{us}, can be computed. We assume η_{aper} of RXs does not change since the beamwidth at the respective f_{sc} of RXs is larger than the widths of RXs. Table III shows an example calculation with a P_L of 3 mW at depths of 6 and 10 cm; η_{us} across widths are also plotted in Fig. 15 for both depths with two optimization methods. The implant with RX width of 0.6 mm has the highest η_{US} for both depths. For 6 cm depth, the ratio of η_{us} across widths between the GM and FP optimizations are 1.1–1.2×; while for 10 cm depth, this increases to 1.5–1.8×. We have also performed measurement at a depth of 6 cm using the transducer with an R_a of 6.8 cm to power up the optogenetic stimulator and compare to the analysis with FP. RX with width of 0.6 mm is selected. By adjusting the input power, a P_L of 3 mW is achieved with a $P_{acou,TX}$ of 168 mW, giving η_{US} of 1.79% compared to 1.93% obtained in the calculation. It can be seen from Table III and Fig. 15 that η_{US} drops for smaller widths because of lower $\eta_{focus,TX}$; η_{US} also decreases for larger widths due to smaller $\eta_{implant}$. Note that f_{sc} of some RXs are not necessarily near the f_{opt} from the TX analysis. For instance, f_{sc} of RX with width of 1.0 mm is at 0.86 MHz while f_{opt} is close to

1.5 MHz with a spherically focused TX with an a of 2 cm; $\eta_{\text{focus,TX}}$ at these two frequencies for the FP method are 3.06% and 4.31%, which are about 1.4× difference. Therefore, one should intelligently design RX to operate at the f_{opt} of a given TX in order to maximize the total efficiency of the link.

VI. Conclusion

We provide a framework to analyze and optimize the efficiency of US links and design miniaturized US-powered implants. Two optimizations, FP and GM, are discussed for the TX analysis; GM, which allows off-focus operation, has higher efficiency than FP. The increase is more pronounced for large depths and smaller TXs. For both methods, a US TX with a larger aperture is more efficient but comes with a tradeoff of alignment sensitivity; operating frequency of 1 to 2 MHz is identified to be the optimal range for powering up miniaturized implants at depths of interest (> 3 cm). Simulations and measurements are performed to verify the analytical framework. In addition, to investigate the scaling of implants, we demonstrate a co-design methodology for RXs and the power recovery chain. PMN-PT is chosen as the material for RXs since its resonance lies in the derived optimal frequency range when scaled down. System-level analysis for the implant efficiency is presented for the application of optogenetic stimulation; the implant efficiency is shown to be highly dependent on the characteristics of RXs and the interface to power electronics. Finally, we show the total US link efficiency by combining both TX and RX analysis; the implant with RX width of 0.6 mm has the highest total link efficiencies of 1.93% and 0.23% using the spherically focused TX with an a of 2 cm and P_{L} of 3 mW at 6 and 10 cm depths when optimized with FP (GM has 2.19% and 0.38%). The measured link efficiency at 6 cm is 1.79%, comparable to the FP optimization.

The techniques introduced in this paper can be applied to different design parameters, such as sizes of TXs and RXs, piezoelectric materials with biocompatible packaging, types of power recovery circuits, or applications with different required power levels, to accurately estimate and optimize the end-to-end US link efficiency while scaling down US-powered implantable devices to smaller form factors. Future works include extending the framework to study the effect of inhomogeneous tissue, implementing a transmitter array, and characterizing the angular response of RXs.

Acknowledgment

The authors thank Prof. Khuri-Yakub at Stanford University for his insight and valuable discussions.

This work was supported in parts by: the DARPA Young Faculty Award under grant number D14AP00043, the NSF CAREER Award under Grant ECCS-1454107, the NSF Graduate Research Fellowships Program under Grant DGE-114747, NIH NIBIB under award number R01EB025867, and Stanford internal seed funds including SystemX Alliance. The content is solely the responsibility of the authors and does not necessarily represent the official views of the NIH.

References

[1]. Famm K, Litt B, Tracey KJ, Boyden ES, and Slaoui M, “Drug discovery: Ajump-start for electroceuticals,” Nature, vol. 496, no. 7444, pp. 159–61, Apr. 2013. [PubMed: 23579662]

[2]. Andreu-Perez J, Leff DR, Ip HMD, and Yang GZ, "From Wearable Sensors to Smart Implants-Toward Pervasive and Personalized Healthcare," IEEE Trans. Biomed. Eng, vol. 62, no. 12, pp. 2750–2762, 2015. [PubMed: 25879838]

[3]. Chen LY et al., "Continuous wireless pressure monitoring and mapping with ultra-small passive sensors for health monitoring and critical care," Nat. Commun, vol. 5, pp. 1–10, 2014.

[4]. Brinton M et al., "Electronic enhancement of tear secretion," J. Neural Eng, vol. 13, no. 1, 2015.

[5]. Rabaey JM et al., "Powering and communicating with mm-size implants," in 2011 Design, Automation & Test in Europe, 2011, pp. 1–6.

[6]. Ho JS et al., "Wireless power transfer to deep-tissue microimplants," Proc. Natl. Acad. Sci. U. S. A, vol. 111, no. 22, pp. 7974–7979, Jun. 2014. [PubMed: 24843161]

[7]. Charthad J, Weber MJ, Chang TC, and Arbabian A, "A mm-Sized Implantable Medical Device (IMD) With Ultrasonic Power Transfer and a Hybrid Bi-Directional Data Link," IEEE J. Solid-State Circuits, vol. 50, no. 8, pp. 1741–1753, Aug. 2015.

[8]. Cheng Y, Wang G, and Ghovanloo M, "Analytical Modeling and Optimization of Small Solenoid Coils for Millimeter-Sized Biomedical Implants," IEEE Trans. Microw. Theory Tech, vol. 65, no. 3, pp. 1024–1035, 2017.

[9]. Jow U and Ghovanloo M, "Design and Optimization of Printed Spiral Coils for Efficient Transcutaneous Inductive Power Transmission," IEEE Trans. Biomed. Circuits Syst, vol. 1, no. 3, pp. 193–202, 2007. [PubMed: 23852413]

[10]. Aldaoud A, Laurenson C, Rivet F, Yuce MR, and Redoute JM, "Design of a miniaturized wireless blood pressure sensing interface using capacitive coupling," IEEE/ASME Trans. Mechatronics, vol. 20, no. 1, pp. 487–491, 2015.

[11]. Liu C, Guo YX, Sun H, and Xiao S, "Design and Safety Considerations of an Implantable Rectenna for Far-Field Wireless Power Transfer," IEEE Trans. AntennasPropag, vol. 62, no. 11, pp. 5798–5806, 2014.

[12]. Mujeeb-U-Rahman M, Adalian D, Chang CF, and Scherer A, "Optical power transfer and communication methods for wireless implantable sensing platforms," J. Biomed. Opt, vol. 20, no. 9, p. 95012, 2015.

[13]. Denisov A and Yeatman E, "Ultrasonic vs. inductive power delivery for miniature biomedical implants," 2010 Int. Conf. Body Sens. Networks, BSN 2010, pp. 84–89, 2010.

[14]. Shahab S and Erturk A, "Contactless ultrasonic energy transfer for wireless systems: acoustic-piezoelectric structure interaction modeling and performance enhancement," Smart Mater. Struct, vol. 23, no. 12, p. 125032, 2014.

[15]. Ozeri S and Shmilovitz D, "Ultrasonic transcutaneous energy transfer for powering implanted devices.," Ultrasonics, vol. 50, no. 6, pp. 556–66, 5 2010. [PubMed: 20031183]

[16]. Mazzilli F, Lafon C, and Dehollain C, "A 10.5 cm ultrasound link for deep implanted medical devices," IEEE Trans. Biomed. Circuits Syst, vol. 8, no. 5, pp. 738–750, Oct. 2014. [PubMed: 25388881]

[17]. Meng M and Kiani M, "Design and Optimization of Ultrasonic Wireless Power Transmission Links for Millimeter-Sized Biomedical Implants," IEEE Trans. Biomed. Circuits Syst, vol. 11, no. 1, pp. 98–107, Feb. 2017. [PubMed: 27662684]

[18]. Chang TC, Weber MJ, Charthad J, Baltsavias S, and Arbabian A, "Scaling of Ultrasound-Powered Receivers for Sub-millimeter Wireless Implants," in IEEE Biomedical Circuits and Systems Conference (BioCAS), 2017, pp. 1–4. [PubMed: 30406220]

[19]. Gelat P, TerHaar G, and Saffari N, "The optimization of acoustic fields for ablative therapies of tumours in the upper abdomen," Phys Med Biol, vol. 57, no. 24, pp. 8471–8497, Dec. 2012. [PubMed: 23207408]

[20]. Goss SA, Johnston RL, and Dunn F, "Comprehensive compilation of empirical ultrasonic properties of mammalian tissues," J. Acoust. Soc. Am, vol. 64, no. 2, pp. 423–457, Aug. 1978. [PubMed: 361793]

[21]. "Information for Manufacturers Seeking Marketing Clearance of Diagnostic Ultrasound Systems and Transducers," Center for Devices and Radiological Health, U.S. FDA, Rockville, MD, 2008.

[22]. Weber MJ, Yoshihara Y, Sawaby A, Charthad J, Chang TC, and Arbabian A, "A Miniaturized Single-Transducer Implantable Pressure Sensor With Time-Multiplexed Ultrasonic Data and Power Links," IEEE J. Solid-State Circuits, vol. 53, no. 4, pp. 1089–1101, 2018.

[23]. Chang TC, Wang ML, Charthad J, Weber MJ, and Arbabian A, "A 30.5mm^3 Fully Packaged Implantable Device with Duplex Ultrasonic Data and Power Links Achieving 95kb/s with <10^{-4} BER at 8.5cm Depth," in IEEE Int. Solid-State Circuits Conf. (ISSCC) Dig. Tech. Papers, 2017, pp. 460–462.

[24]. Weber MJ, Bhat A, Chang TC, Charthad J, and Arbabian A, "A Miniaturized Ultrasonically Powered Programmable Optogenetic Stimulator System," in IEEE Topical Conf. Biomedical Wireless Technology, Networks, Sensing System, 2016, pp. 12–14.

[25]. Seo D et al., "Wireless Recording in the Peripheral Nervous System with Ultrasonic Neural Dust Neuron NeuroResource Wireless Recording in the Peripheral Nervous System with Ultrasonic Neural Dust," Neuron, vol. 91, no. 3, pp. 1–11, Aug. 2016. [PubMed: 27387643]

[26]. Zhou J, Kim A, Song SH, and Ziaie B, "An ultrasonically powered implantable micro-light source for localized photodynamic therapy," 2015 Transducers - 2015 18th Int. Conf. Solid-State Sensors, Actuators Microsystems, TRANSDUCERS 2015, pp. 876–879, 2015.

[27]. Charthad J et al., "A mm-sized wireless implantable device for electrical stimulation of peripheral nerves," IEEE Trans. Biomed. Circuits Syst, vol. 12, no. 2, pp. 257–270, 2018. [PubMed: 29578414]

[28]. Lawry TJ, Wilt KR, Scarton HA, and Saulnier GJ, "Analytical modeling of a sandwiched plate piezoelectric transformer-based acoustic-electric transmission channel," IEEE Trans. Ultrason. Ferroelectr. Freq. Control, vol. 59, no. 11, pp. 2476–2486, 2012. [PubMed: 23192811]

[29]. Kim S, Ho JS, and Poon ASY, "Wireless Power Transfer to Miniature Implants: Transmitter Optimization," IEEE Trans. Antennas Propag, vol. 60, no. 10, pp. 4838–4845, 2012.

[30]. Chang TC, Weber MJ, Wang ML, Charthad J, Khuri-yakub BT, and Arbabian A, "Design of Tunable Ultrasonic Receivers for Efficient Powering of Implantable Medical Devices with Reconfigurable Power Loads," IEEE Trans. Ultrason. Ferroelectr. Freq. Control, vol. 63, no. 10, pp. 1554–1562, Oct. 2016. [PubMed: 27623580]

[31]. Fleury G, Berriet R, LeBaron O, Huguenin B, and France I, "New piezocomposite transducers for therapeutic ultrasound," SPIE, vol. 4954, pp. 227–235, 2003.

[32]. "H-Transducer Series," Sonic Concepts, Woodenville, WA.

[33]. Wygant IO et al., "An integrated circuit with transmit beamforming flip-chip bonded to a 2-D CMUT array for 3-D ultrasound imaging," IEEE Trans. Ultrason. Ferroelectr. Freq. Control, vol. 56, no. 10, pp. 21452156, 2009. [PubMed: 19942502]

[34]. El-Desouki MM and Hynynen K, "Driving circuitry for focused ultrasound noninvasive surgery and drug delivery applications," Sensors, vol. 11, no. 1 pp. 539–556, 2011. [PubMed: 22346589]

[35]. Kino GS, Sound Wave Propagation. Englewood Cliffs, NJ, USA: Prentice-Hall, 1987.

[36]. Szabo TL, "Diagnostic Ultrasound Imaging: Inside Out," Diagnostic Ultrasound Imaging: Inside Out, vol. 787 pp. 735–763, 2014.

[37]. Jensen JA, "FIELD: A Program for Simulating Ultrasound Systems," Med. Biol. Eng. Comput, vol. 34, no. SUPPL. 1, pp. 351–352, 1996. [PubMed: 8945858]

[38]. Jensen JA and Svendsen NB, "Calculation of Pressure Fields from Arbitrarily Shaped, Apodized, and Excited Ultrasound Transducers," IEEE Trans. Ultrason. Ferroelectr. Freq. Control, vol. 39, no. 2, pp. 262—267, 1992. [PubMed: 18263145]

[39]. Smith SW, Pavy HG, and vonRamm OT, "High-Speed Ultrasound Volumetric Imaging System—Part I: Transducer Design and Beam Steering," IEEE Trans. Ultrason. Ferroelectr. Freq. Control, vol. 38, no. 2, pp. 100–108, 1991. [PubMed: 18267563]

[40]. Kossoff G, "Analysis of focusing action of spherically curved transducers," Ultrasound Med. Biol, vol. 5, no. 4, pp. 359–365, 1979. [PubMed: 531991]

[41]. Huang JH and Ding D, "A simple approximate formula for the physical focal length of spherically focused transducers," IEEE Trans. Ultrason. Ferroelectr. Freq. Control, vol. 56, no. 12, pp. 2764–2768, 2009. [PubMed: 20040414]

[42]. Goldstein A, "Steady State Spherically Focused, Circular Aperture Beam Patterns," Ultrasound Med. Biol, vol. 32, no. 10, pp. 1441–1458, Jun. 2006. [PubMed: 17045863]

[43]. Wang M, Chang TC, Teisberg T, Weber M, Charthad J, and Arbabian A, “Closed-loop ultrasonic power and communication with multiple miniaturized active implantable medical devices,” 2017 IEEE Int. Ultrason. Symp, pp. 7–10, 2017.

[44]. Lerch TP, Schmerr LW, and Sedov A, “Characterization of spherically focused transducers using an ultrasonic measurement model approach,” Res. Nondestruct. Eval, vol. 8, no. 1, pp. 1–21, 1996.

[45]. Liske H, Qian X, Anikeeva P, Deisseroth K, and Delp S, “Optical control of neuronal excitation and inhibition using a single opsin protein, ChR2,” Sci. Rep, vol. 3, pp. 2–8, 2013.

[46]. “TRS X2B Material Constants,” TRS Technologies, State College, PA.

[47]. Kossoff G, “The Effects of Backing and Matching on the Performance of Piezoelectric Ceramic Transducers,” IEEE Trans. Sonics Ultrason, vol. 13, no. 1, pp. 20–30, 1966.

[48]. Kunkel HA, Locke S, and Pikeroen B, “Finite-Element Analysis of Vibrational Modes in Piezoelectric Ceramic Disks,” IEEE Trans. Ultrason. Ferroelectr. Freq. Control, vol. 37, no. 4, pp. 316–328, Jul. 1990. [PubMed: 18285047]

[49]. Balanis CA, Antenna Theory: Analysis and Design, 3rd ed. Hoboken, NJ: Wiley, 2005.

[50]. Zumofen G, Mojarad NM, Sandoghdar V, and Agio M, “Perfect reflection of light by an oscillating dipole,” Phys. Rev. Lett, vol. 101, no. 18, pp. 1–4, 2008.

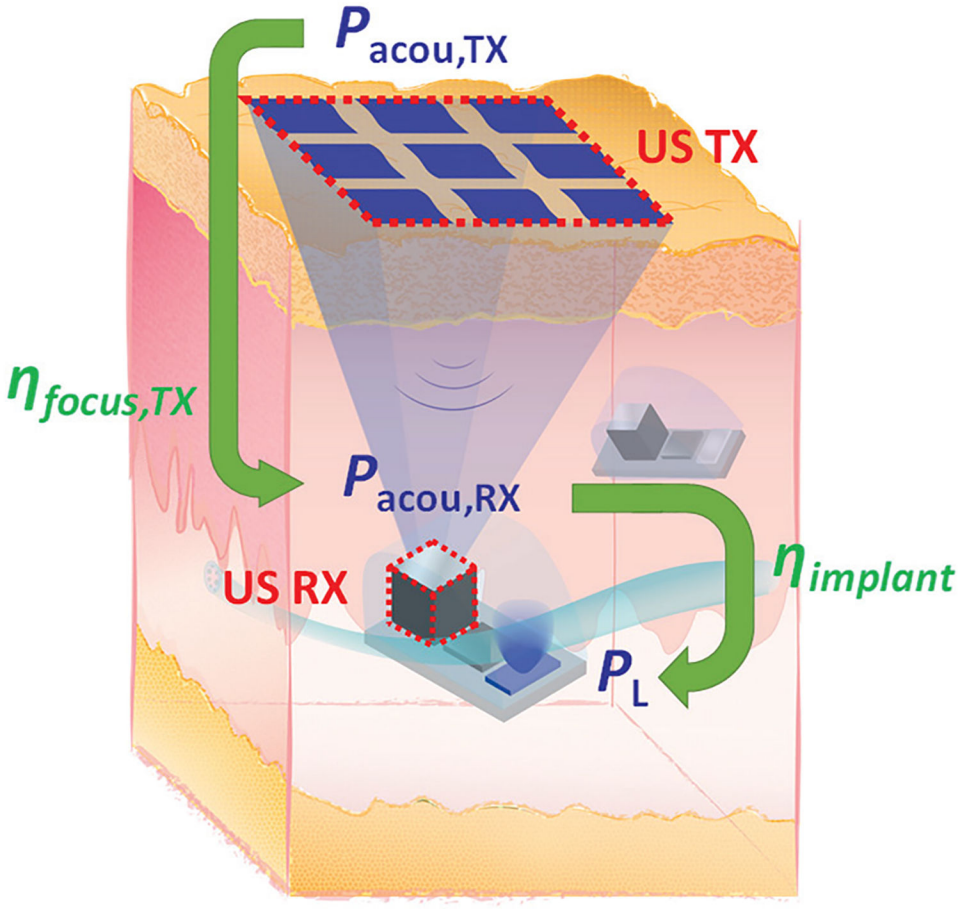

Fig. 1.
A conceptual diagram of an implant system with US wireless power transfer.

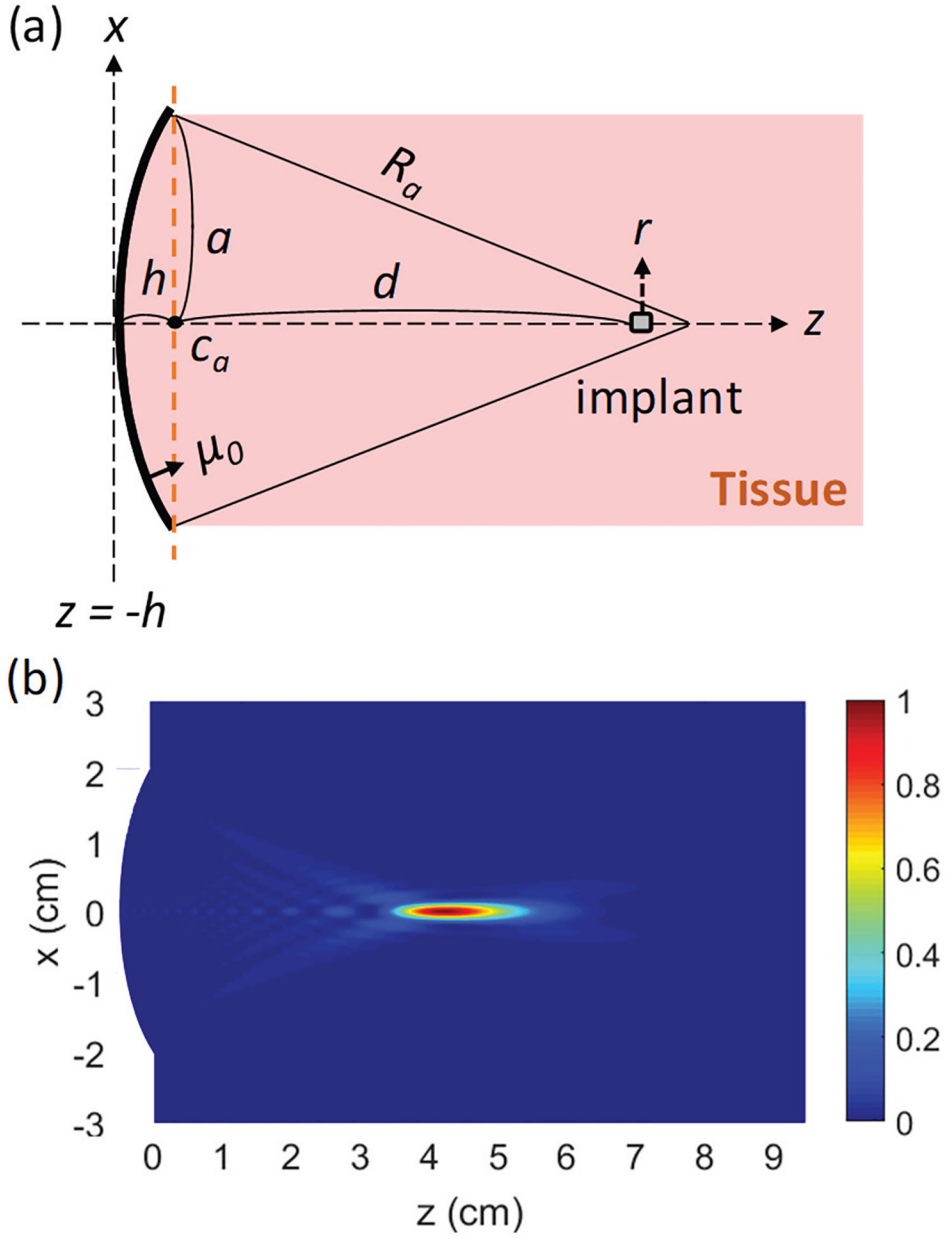

Fig. 2.

(a) Side view of a generic spherically focused transducer with a circular aperture of a and a uniform normal displacement velocity of μ_0 on the surface, (b) Simulated normalized I_{acou} in the xz plane at 1.0 MHz with a = 2 cm, R_a = 5 cm, and μ_0 = 5 mm/s in tissue which has a density of 1 g/cm^3 and an attenuation ofθ.8 dB/cm. The color scaleis linear.

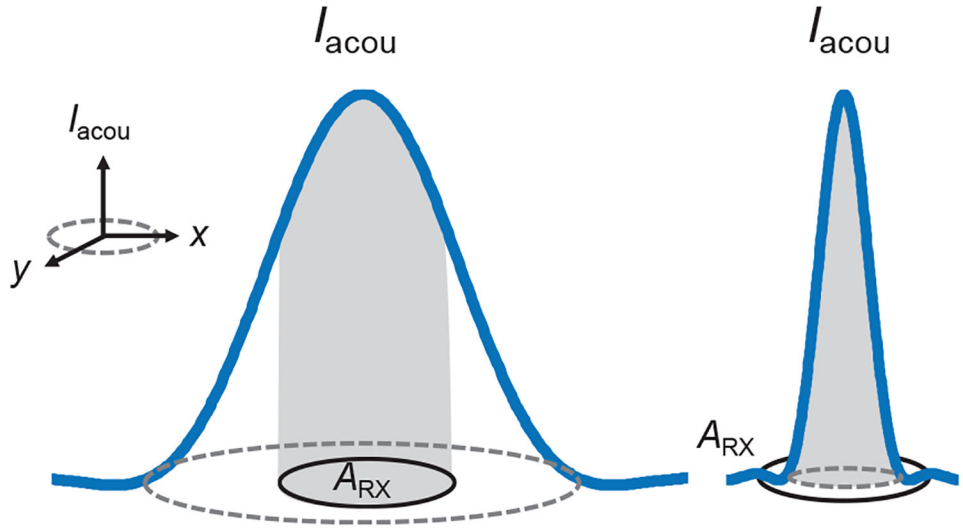

Fig. 3.

Cone model used for $P_{acou,RX}$ calculation. The bottom of the cone is the plane of interest (xy-plane) and the tip of the cone is the maximum I_{acou} in the plane. The volume of the cone represents the total acoustic power in the beam. The shaded volume is the acoustic power captured by the receiver with A_{RX}.

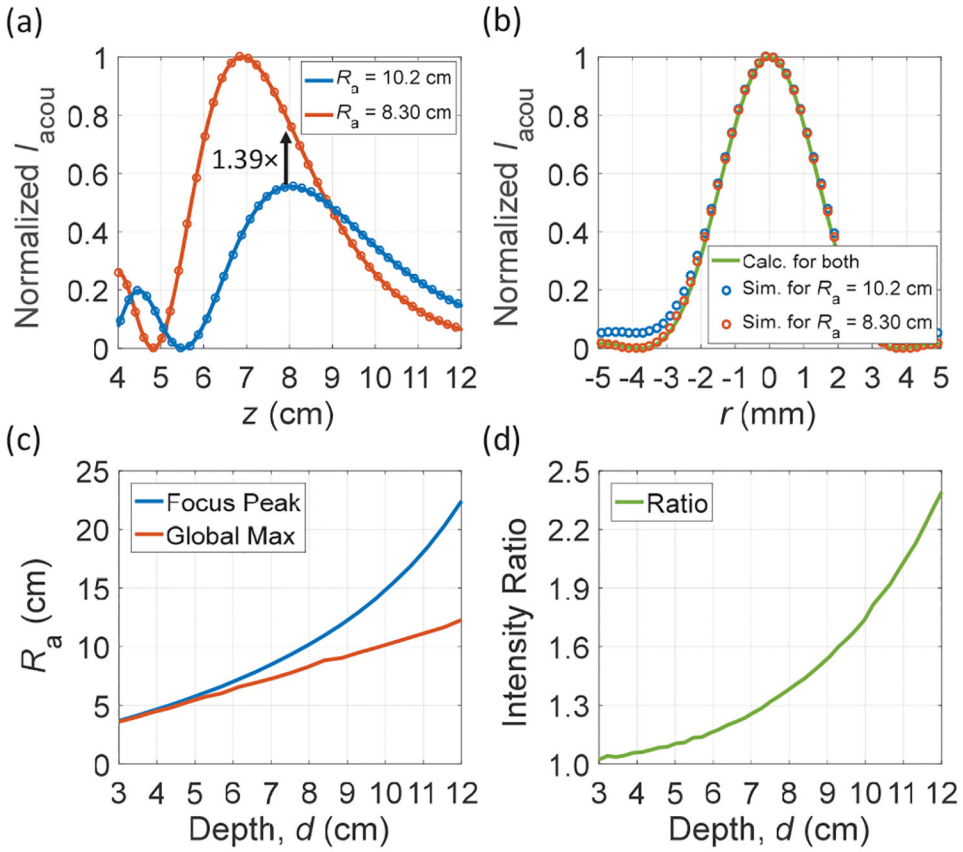

Fig. 4.

(a) Calculated (solid lines) and simulated (circle markers) normalized I_{acou} vs. depth with two different R_a. (b) Calculated and simulated beam profiles at 8 cm depth, (c) Comparison of R_a for FP and GM vs. targeted depths, (d) Calculated intensity ratio between FP and GM across depths. Parameters used are a = 2 cm, μ_0 = 5 mm/s, c_0 = 1540 m/s, and α = 0.8 dB/cm; the operating frequency is 1.0 MHz.

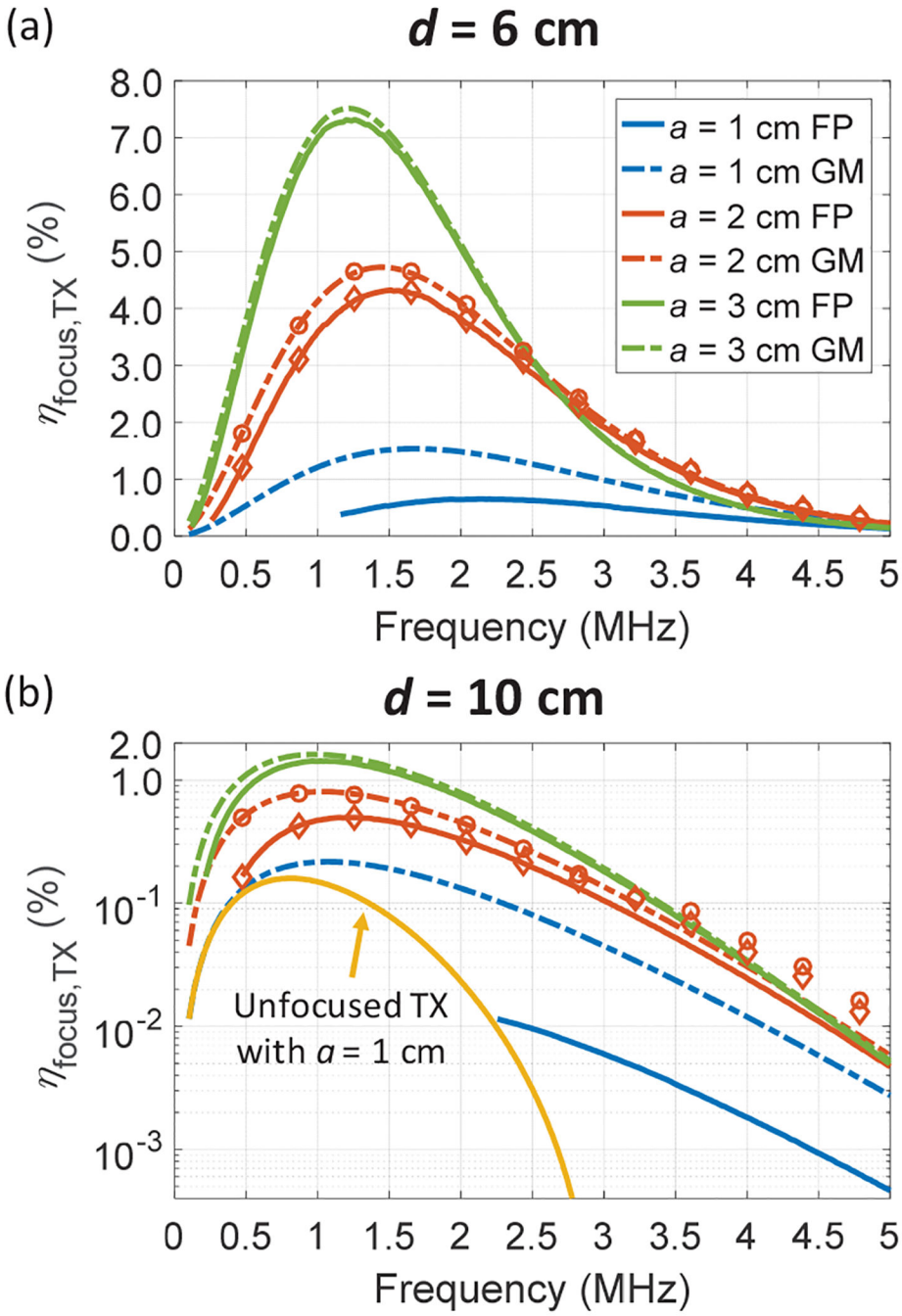

Fig. 5.

Calculated $\eta_{focus,TX}$ vs. frequency for 3 different a and for depths of (a) 6 cm and (b) 10 cm with an A_{RX} of 1 mm^2. Solid line is optimized with FP and dash line is with GM. For the FP method, the TX with a = 1.0 cm for a depth of 10 cm is not able tofocus for lower frequencies; $\eta_{focus,TX}$ for a plane transducer is also shown in (b). Simulated $\eta_{focus,TX}$for a = 2.0 cm are plotted with diamond (FP) and circle (GM) markers.

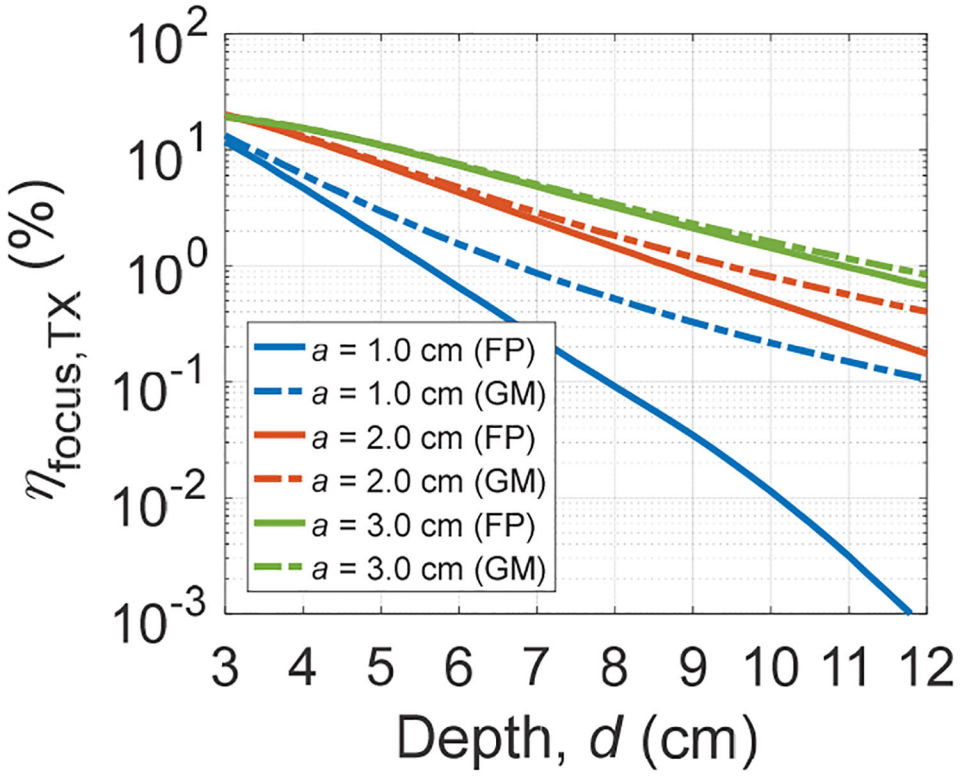

Fig. 6.

Calculated optimal $\eta_{focus,TX}$ for three different a across transmission depths from 3 to 12 cm with an A_{RX} of 1 mm^2 for the FP and GM optimizations.

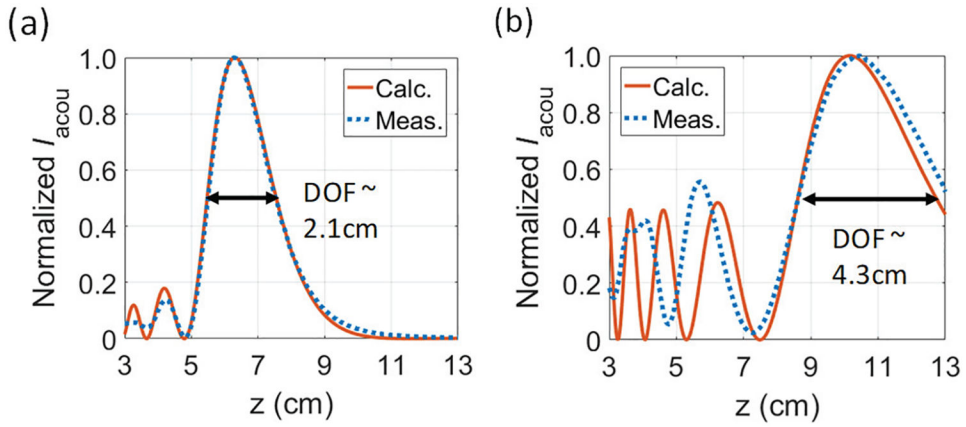

Fig. 7.

Measured (500 μm step size) and calculated normalized I_{acou} in castor oil for TXs with (a) an R_a of 6.8 cm at 1.20 MHz and (b) an R_a of 12.5 cm at 1.40 MHz.

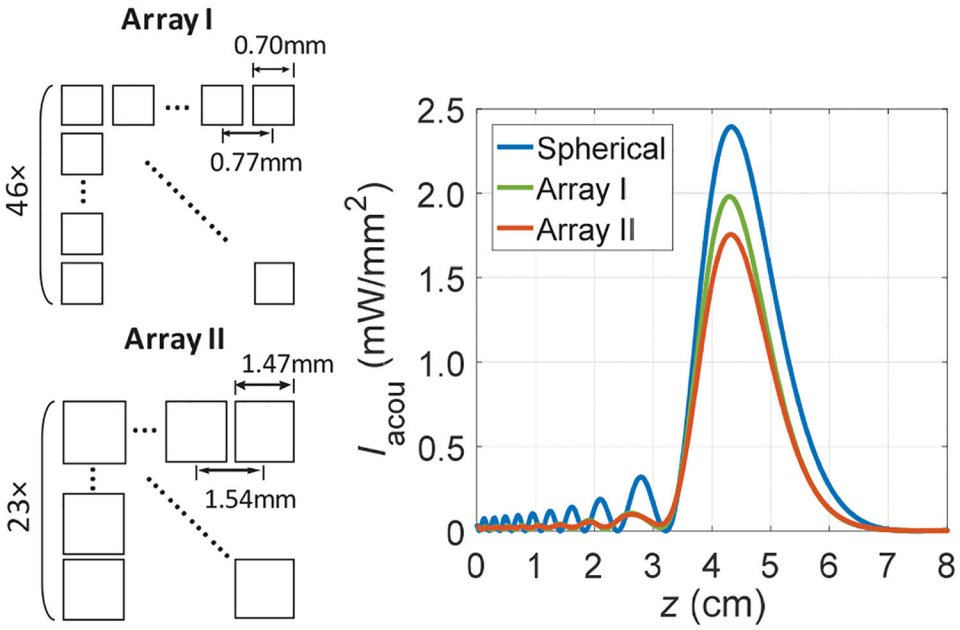

Fig. 8.

Illustrations of two arrays (not to scale) and comparisons of I_{acou} along the z axis for a spherically focused transducer with an a of 2 cm, array I (46 × 46), and array II (23 × 23) in the simulation.

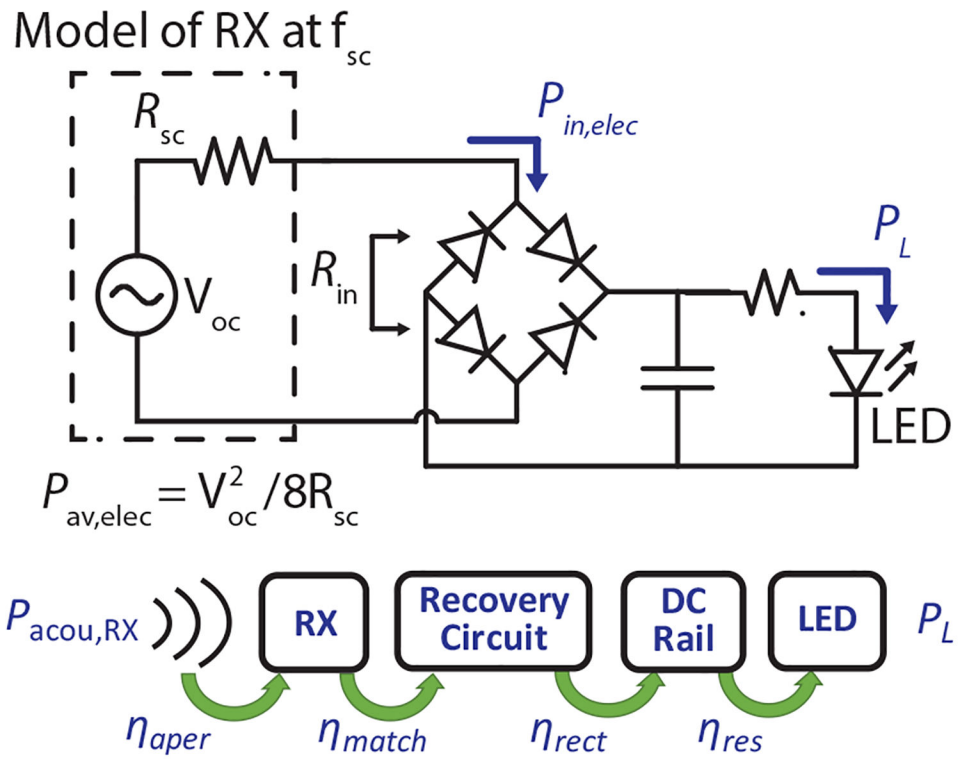

Fig. 9.

Circuit schematics of a US-powered optogenetic stimulator. The corresponding efficiency terms in (8) are illustrated with the flow diagram.

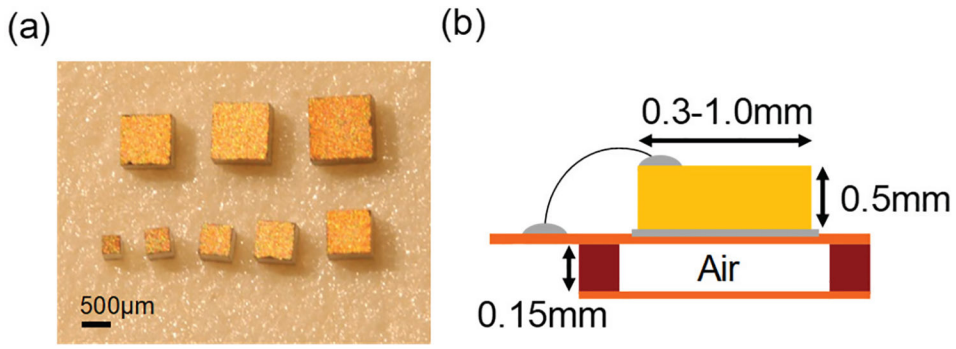

Fig. 10.

(a) Photo of RXs made from PMN-PTs with thickness of 0.5 mm and widths ranging from 0.3 mm to 1.0 mm. (b) Diagram of the measurement package built on flexible PCB. The package is immersed in mineral oil during measurement (modified from [18]).

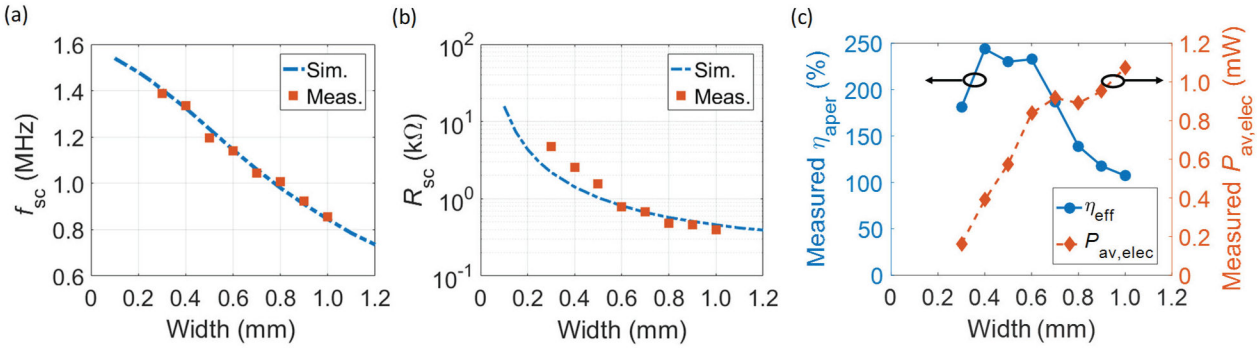

Fig. 11.

Simulated and measured (a) f_{sc} versus width and (b) R_{sc} versus width of PMN-PT RXs with thickness of 0.5 mm. (c) Measured η_{aper} and $P_{av,elec}$ with I_{acou} of 1 mW/mm^2 [18].

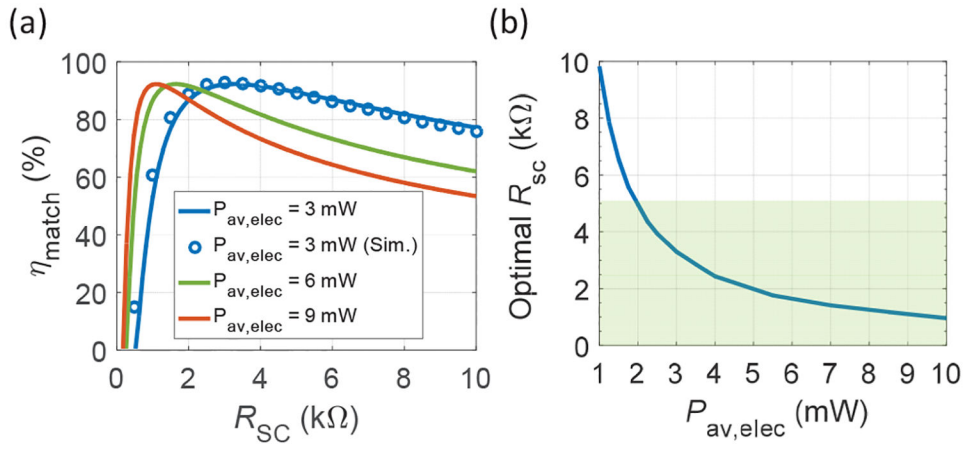

Fig. 12.

(a) Calculated η_{match} as a function of R_{sc} at three different $P_{av,elec}$. $P_{av,elec}$ of 3 mW with SPICE simulation matches the calculation, (b) Optimal R_{sc} for $P_{av,elec}$ from 1 to 10 mW. The shaded region corresponds to the R_{sc} of RXs (modified from [18]).

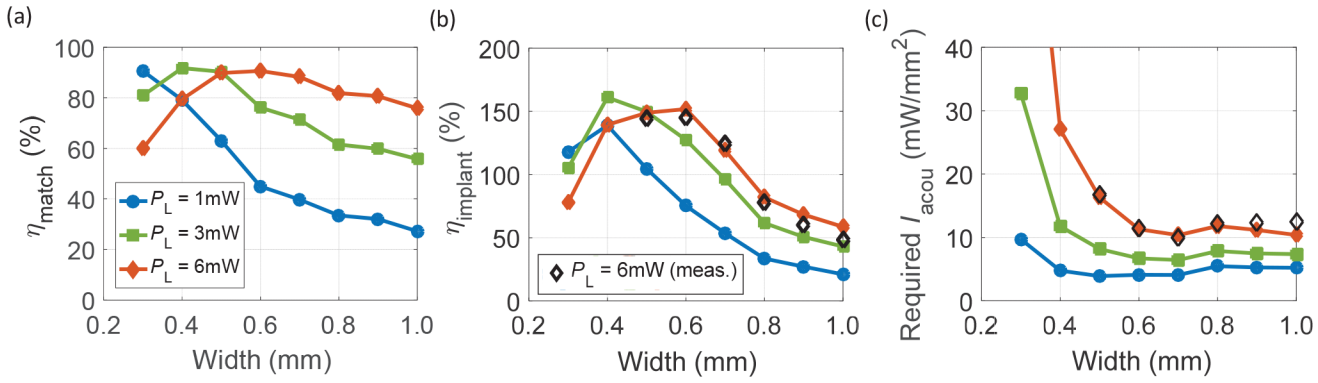

Fig. 13.

(a) Calculated η_{match} versus width for different P_L based on the measured R_{sc} of each RX. (b) Calculated $\eta_{implant}$ and (c) minimum required I_{acou} versus width for different P_L based on the measured R_{sc} and η_{aper} of each RX. Measurement for P_L of 6 mW is also shown in (b) and (c). For RXs with width of 0.3 mm and 0.4 mm, I_{acou} required for P_L of 6 mW exceeds the limit of the measurement setup; thus, measured data points are omitted. Legends in (a) and (b) apply to all three plots (modified from [18]).

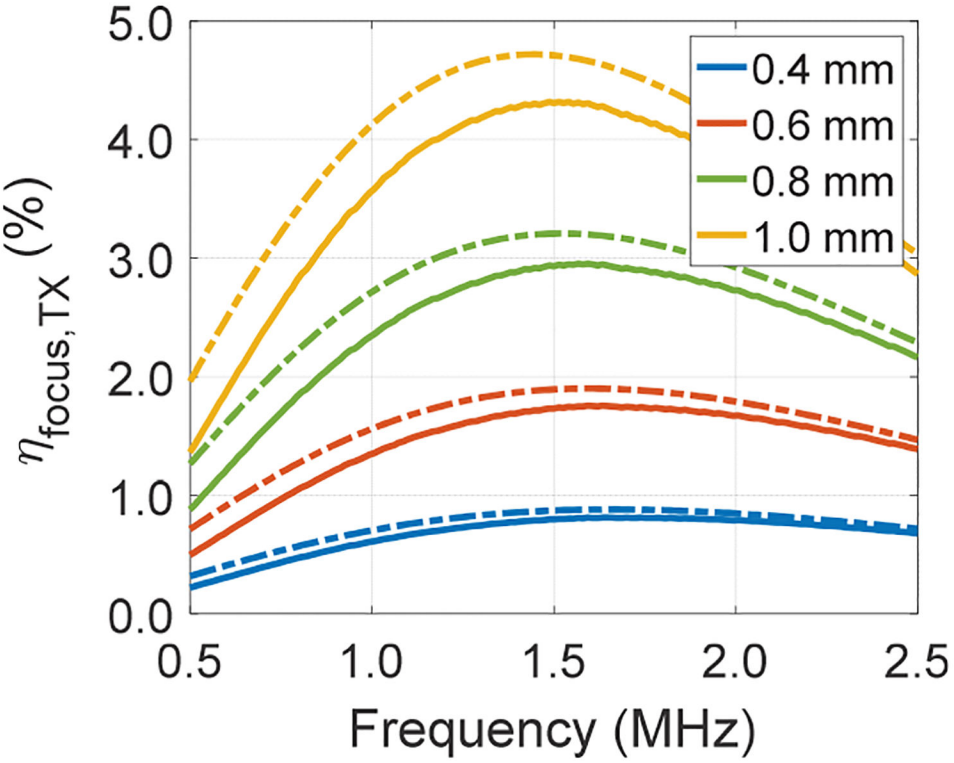

Fig. 14.

Calculated $\eta_{focus,TX}$ for both the FP (solid) and GM (dash) methods using a spherically focused TX with an a of 2 cm across different RX widths at a depth of 6 cm.

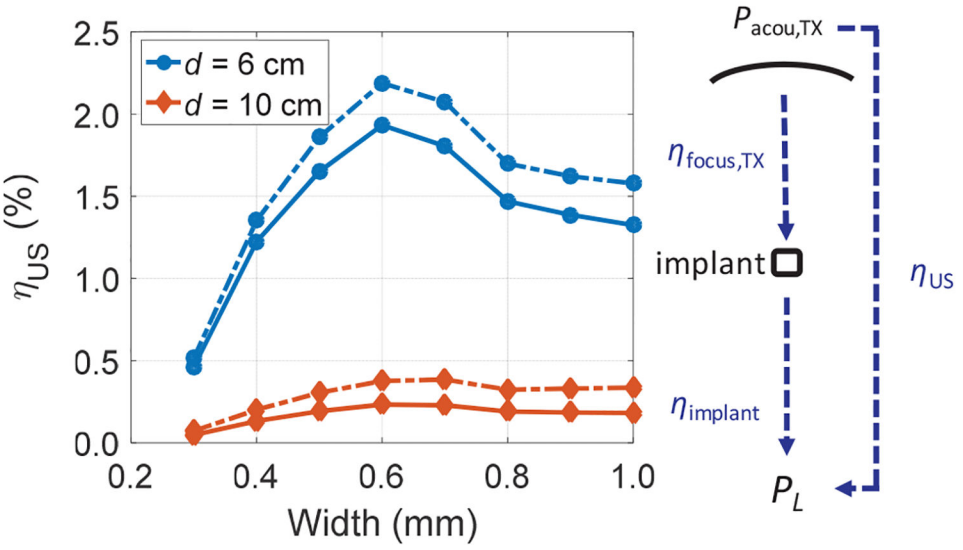

Fig. 15.

Calculated total US link efficiency, η_{us}, using (1) for a spherically focused TX with an *a* of 2 cm across different RX widths at depths of 6 cm and 10 cm. Solid line is optimized with FP and dash line is with GM.

TABLE I

Detail Summary at the Optimal Points in Fig. 5

		f_{opt} (MHz)		$\eta_{focus,TX}$ (%)		R_a (cm)		w_{3dB} (mm) [calc./sim.]	
Depth (cm)		6	10	6	10	6	10	6	10
a = 1.0 cm	FP	2.16	0.82 *	0.65	0.16 *	10.1	×	2.13/2.24	9.33/9.48 *
	GM	1.69	1.08	1.54	0.22	6.40	10.7	2.72/2.76	7.08/7.10
a = 2.0 cm	FP	1.51	1.22	4.32	0.50	6.64	13.2	1.52/1.60	3.14/3.28
	GM	1.45	1.04	4.72	0.81	6.31	10.2	1.58/1.65	3.68/3.76
a = 3.0 cm	FP	1.26	1.02	7.32	1.43	6.80	11.1	1.21/1.33	2.50/2.64
	GM	1.22	0.98	7.51	1.62	6.70	10.5	1.25/1.40	2.60/2.72

* Plane transducer, off-focus operation.

TABLE II

Piezoelectric Material Peoperties [35], [46]

	PMN-PT	**PZT4**	**PZT5H**
Density, ρ (kg/m^3)	8000	7500	7500
Sound Velocity, v_p (m/s)	3480	4100	3850
Acoustic Impedance, Z_c (MRayls)	27.8	30.8	28.9
Electrical-Mechnical Coupling Coefficient, k_{33}	0.91	0.70	0.75
Relative Dielectric Constant, ε^T_{33}	5400	1300	3400
Calculated f_{sc} for $t = 0.5$ mm (MHz)	1.57	3.07	2.69

TABLE III

US Link Efficiency for a Load power of 3 mW at the Resonance of RXs Using the with a Circular Aperture size of 2 cm

	f_{sc} (MHz)	$\eta_{implant}$ (%)	$\eta_{focus,TX}$ (%) [FP/GM]		η_{US} (%) [FP/GM]		w_{3dB} (mm) calc.	
Width (mm)			**6 cm**	**10 cm**	**6 cm**	**10 cm**	**6 cm**	**10 cm**
0.3	1.39	105	0.44 0.49	0.046 0.069	0.46 0.51	0.048 0.073	1.65	2.75
0.4	1.34	161	0.76 0.84	0.08 0.13	1.22 1.35	0.13 0.20	1.71	2.85
0.5	1.20	150	1.10 1.24	0.13 0.20	1.65 1.86	0.19 0.30	1.91	3.19
0.6	1.14	128	1.50 1.71	0.18 0.29	1.93 2.19	0.23 0.38	2.01	3.36
0.7	1.04	96	1.88 2.16	0.24 0.40	1.80 2.07	0.23 0.39	2.21	3.68
0.8	1.01	62	2.37 2.74	0.30 0.52	1.47 1.70	0.19 0.32	2.27	3.79
0.9	0.92	51	2.72 3.18	0.36 0.65	1.39 1.62	0.19 0.33	2.49	4.16
1.0	0.86	43	3.08 3.67	0.42 0.78	1.32 1.58	0.18 0.34	2.67	4.45

* ηUS are calculated values based on ηimplant and ηfocus,TX.